Electrochemistry
The Electrochemical Society of Japan
Received: November 30, 2016
Accepted: April 11, 2017
Published: July 5, 2017
http://dx.doi.org/10.5796/electrochemistry.85.391
Article
Electrochemistry, **85(7)**, 391–396 (2017)

Structural and Electrochemical Properties of Hard Carbon Negative Electrodes for Sodium Secondary Batteries Using the Na[FSA]–[C_3C_1pyrr][FSA] Ionic Liquid Electrolyte

Takayuki YAMAMOTO,[a] Tetsuji YAMAGUCHI,[a] Toshiyuki NOHIRA,[b,*] Rika HAGIWARA,[a,*] Atsushi FUKUNAGA,[c] Shoichiro SAKAI,[c] and Koji NITTA[c]

[a] *Graduate School of Energy Science, Kyoto University, Yoshida-honmachi, Sakyo-ku, Kyoto 606-8501, Japan*
[b] *Institute of Advanced Energy, Kyoto University, Gokasho, Uji 611-0011, Japan*
[c] *Sumitomo Electric Industries, Ltd., 1-1-3 Shimaya, Konohana-ku, Osaka 554-0024, Japan*

* *Corresponding authors: nohira.toshiyuki.8r@kyoto-u.ac.jp, hagiwara@energy.kyoto-u.jp*

ABSTRACT

Two kinds of hard carbon (HC) were investigated as negative electrodes for sodium secondary batteries using Na[FSA]–[C_3C_1pyrr][FSA] as an ionic liquid electrolyte at 363 K. The structural properties of HCs were studied by X-ray diffraction (XRD), Raman spectroscopy, small-angle X-ray scattering (SAXS), and field-emission scanning electron microscopy (FE-SEM). The interlayer distance between graphene sheets and the pore size were different for these HCs. Potential slope and plateau regions were observed in charge–discharge curves, which is typical for HC negative electrodes. More detailed examinations revealed that the HC with a larger interlayer distance showed higher capacity in the slope region, while that with a larger pore size exhibited a higher capacity in the plateau region. Finally, the rate capabilities and cycling properties of HC negative electrodes were evaluated.

© The Electrochemical Society of Japan, All rights reserved.

Keywords : Sodium Secondary Battery, Ionic Liquid, Hard Carbon, Negative Clectrode

1. Introduction

The establishment of a low-carbon society is an urgent task to mitigate global warming and climate change. A promising solution is the combination of renewable energy generation and large-scale electrical energy storage (EES) devices. Lithium-ion batteries (LIBs) are good candidates for EES devices because they possess high energy densities and are already used in a wide variety of small electronic devices like PC laptops and smartphones. Currently, the demand for large-scale LIBs is increasing. However, future price hikes and supply instability are possible, because the lithium and cobalt resources are not abundant and are unevenly distributed in the world. Moreover, conventional LIB electrolytes contain volatile and flammable organic solvents, causing safety concerns, especially for large-scale batteries.

Our group focused on the development of sodium secondary batteries using ionic liquid electrolytes to resolve the aforementioned problems.[1–11] Sodium is abundant in the crust and seawater, showing a relatively low standard redox potential (−2.71 V vs. SHE). Thus, batteries with low cost and high energy density can be constructed. Moreover, ionic liquids are inherently safe due to their negligible volatility and non-flammability, with some of them showing reasonably high ionic conductivities and wide electrochemical windows.[5,6]

We have already reported that Na[TFSA]–Cs[TFSA] (TFSA = bis(trifluoromethylsulfonyl)amide) and Na[FSA]–K[FSA] (FSA = bis(fluorosulfonyl)amide) ionic liquids are promising electrolytes for sodium secondary batteries operating at an intermediate temperature range (>353 K).[1–4] However, these salts are solid at room temperature, while electrolytes with lower melting points are more desirable for the construction of batteries for a wide range of practical applications. Recently, we developed a new electrolyte, Na[FSA]–[C_3C_1pyrr][FSA] (C_3C_1pyrr = *N*-methyl-*N*-propylpyrrolidinium), that is a liquid in a wide temperature range, including room temperature.[5,6] For example, several positive electrode materials like $NaCrO_2$ and $Na_{2-x}Fe_{1+x/2}P_2O_7$ exhibited good charge–discharge performances in Na[FSA]–[C_3C_1pyrr][FSA] at 253–363 K.[5,7–9] We have also investigated the charge–discharge behavior of hard carbon (HC) negative electrodes in this ionic liquid at 363 K.[10,11]

HC is mainly composed of two structural domains, i.e., randomly-arranged graphene domains and their interstitial sites (pores), and its charge–discharge behavior as a negative electrode material for sodium secondary batteries has been well investigated in organic solvent electrolytes.[12–20] However, there have been few studies on the correlation of HC structure and its electrochemical behavior in ionic liquid electrolytes.

In the present study, the charge–discharge behavior of two HC negative electrode materials was evaluated for sodium secondary batteries using the Na[FSA]–[C_3C_1pyrr][FSA] ionic liquid electrolyte at 363 K. The relation between structural and electrochemical properties of HC was discussed based on the results of X-ray diffraction (XRD), Raman spectroscopy, small-angle X-ray scattering (SAXS), and field-emission scanning electron microscopy (FE-SEM).

2. Experimental

2.1 Reagents and their handling

Na[FSA] (> 99+%; Mitsubishi Materials Electronic Chemicals Co., Ltd.) and [C_3C_1pyrr][FSA] (> 99.9%; Kanto Chemical Co., Inc.) were dried under vacuum at 353 and 333 K, respectively, for 48 h prior to use. The Na[FSA]–[C_3C_1pyrr][FSA] ionic liquid (20:80 mol%) was prepared by mixing Na[FSA] and [C_3C_1pyrr][FSA] in an argon-filled glove box.

A slurry was prepared by mixing HC powders (CARBOTRON P, Kureha Battery Materials Japan Co., Ltd. (denoted as HC-1); or Sumitomo Bakelite Co., Ltd. (denoted as HC-2)), *N*-methyl-2-pyrrolidone (NMP; Wako Pure Chemical Industries, Ltd.), and the polyamide-imide (PAI; SOXR-O, 18.96 wt% NMP solution, Nippon Kodoshi Corporation) binder (HC:PAI = 96:4 wt%). The slurry was used to coat aluminum foil, and NMP was removed by drying in

vacuum at 353 K for 12 h and subsequently at 473 K for 2 d. The loading mass of HC was between 3.6 and 4.2 mg cm^{-2}.

2.2 Electrochemical measurements and analysis

Electrochemical measurements (VSP, Bio-Logic Co.) were conducted for a 2032-type two-electrode coin cell under an argon atmosphere. A two-ply glass-fiber filter paper (Whatman, GF-A, 260 µm) was used as a separator and was vacuum-impregnated with the electrolyte prior to the test. The working and counter electrodes were the HC electrode and Na metal (99.85%; Sigma-Aldrich, Inc.), respectively. Charge–discharge rates were set at current densities of 25–2000 mA (g-HC)$^{-1}$. The voltage range and temperature of charge–discharge tests were fixed at 0.005–1.200 V and 363 K, respectively.

Galvanostatic intermittent titration technique (GITT) was conducted as follows:

1. Galvanostatic electrolysis was conducted at a constant current density of 25 mA (g-HC)$^{-1}$ for 60 min.
2. The open circuit potential was monitored; when the rate of potential change fell below 1.0 mV h^{-1}, the potential was regarded as being at equilibrium.
3. Steps 1 and 2 were repeated until the charge curve reached 0.005 V in the step 1.

The interlayer distances between the graphene sheets (d_{002}) and the *c*-axis crystallite sizes (L_c) of HC powders were analyzed by XRD using an X-ray diffractometer (SmartLab, Rigaku Co.; Cu-K_α radiation ($\lambda = 0.15418$ nm)). Each HC powder was pulverized using a mortar and pestle to pass through a 150 mesh (100 µm) sieve, and was mixed with silicon powder (>99.999%) in a weight ratio of 90:10. The obtained X-ray diffraction pattern of the mixed powder was corrected using the Lorentz-polarization factor. The evaluations of d_{002} and L_c were conducted using the Gakushin method.[21,22] The small-angle X-ray scattering (SAXS) patterns of HC powders were obtained by the same X-ray diffractometer, and their pore size distribution and average pore diameter (D_{pore}) were calculated using the software NANO-Solver (Rigaku Co.). The *R* values and the *a*-axis crystallite sizes (L_a) of HC powders were evaluated by Raman spectroscopy (Nanofinder 30, Tokyo Instruments) using a He–Ne laser ($\lambda = 633$ nm). The morphologies of HC powders were observed by a field emission scanning electron microscope (FE-SEM; SU-8020, Hitachi).

3. Results and Discussion

3.1 Characterization of HC powders

3.1.1 Evaluation of d_{002}, L_c, and N_{stack} by XRD

Figure 1 shows X-ray diffraction patterns of HC-1 and HC-2.

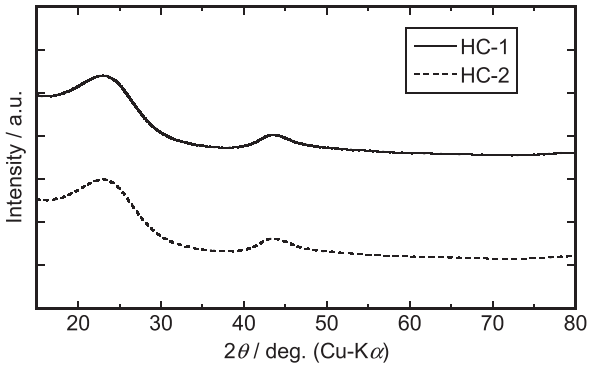

Figure 1. XRD patterns of HC-1 and HC-2.

The 002 diffraction angle (θ_{002}) was determined by the Gakushin method. Subsequently, the values of d_{002} and L_c were obtained from the Bragg equation (Eq. (1)) and the Scherrer equation (Eq. (2)), respectively:

$$\lambda = 2d_{002} \sin\theta_{002} \quad (1)$$

$$L_c = \frac{K\lambda}{\beta \cos\theta_{002}} \quad (2)$$

where λ is the X-ray wavelength (0.15418 nm), K is the shape factor (1.00), and β is the full width at half maximum of the 002 diffraction peak. In addition, the average stack number of graphene sheets (N_{stack}) was calculated as follows:

$$N_{stack} = \frac{L_c}{d_{002}} + 1 \quad (3)$$

The d_{002}, L_c, and N_{stack} values for HC-1 and HC-2 are summarized in Table 1. Both HC-1 and HC-2 possess d_{002} values of ~0.36 nm, which is much larger than that of graphite (0.3354 nm); however, HC-1 shows a slightly larger d_{002} value than HC-2. The L_c and N_{stack} values are ~1.7 nm and 5.5, respectively, for both HC-1 and HC-2. Similar L_c and N_{stack} values were obtained by other groups.[23,24]

3.1.2 Raman spectroscopy

Figure 2 shows the Raman spectra of HC-1 and HC-2, with solid lines depicting the curves obtained by Lorentzian fitting. Both HC-1 and HC-2 show two main peaks around 1340 and 1580 cm^{-1}, corresponding to D- and G-bands, respectively. In addition, as a result of the Lorentzian fitting, a small peak appears at approximately 1500 cm^{-1}, denoted as the P-band and indicating the existence of five-membered rings.[25] The *R* value is usually defined by the ratio of D- and G-band peak intensities, and the *a*-axis crystallite size (L_a) of HC-1 and HC-2 is calculated by the following equation:[26,27]

Table 1. Summary of structural and electrochemical properties of HCs.

	X-ray diffraction			Raman spectroscopy		SAXS	Charge–discharge test	
	d_{002}/nm	L_c/nm	N_{stack}	*R*	L_a/nm	D_{pore}/nm	Q_{slope} /mAh g^{-1}	$Q_{plateau}$ /mAh g^{-1}
HC-1	0.3671(3)	1.68(3)	5.58(7)	1.32	29.1	1.22	83.1	174
HC-2	0.3647(17)	1.66(3)	5.54(5)	1.37	28.1	1.31	68.3	224

d_{002}: Interlayer distance.
L_c: Crystalline size in *c*-axis direction.
N_{stack}: Average stack number of graphene.
R (= $I_{Disorder}/I_{Graphite}$): Intensity ratio of peaks from disordered carbon and graphite-like carbon.
L_a: Crystalline size in *a*-axis direction.
D_{pore}: Average of pore diameter.
Q_{slope}: Capacity of slope region.
$Q_{plateau}$: Capacity of plateau region.

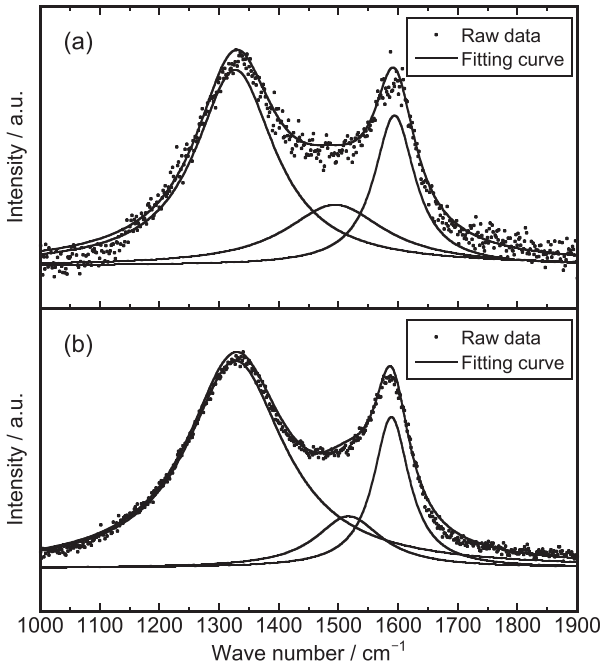

Figure 2. Raman spectra of HC powders. (a) HC-1 and (b) HC-2. Fitting curves are drawn by Lorentz fuction.

$$L_a = (2.4 \times 10^{-10})\lambda_{\text{laser}}^4 \left(\frac{I_D}{I_G}\right)^{-1} \quad (4)$$

where λ_{laser} is the wavelength of the He–Ne laser (633 nm), and I_D and I_G refer to the peak intensities of D- and G-bands, respectively. Both HC-1 and HC-2 show similar values of 1.3–1.4 for R and ~30 nm for L_a (Table 1).

3.1.3 Evaluation of D_{pore} by SAXS

Figure 3a shows the SAXS patterns of HC-1 and HC-2. Slightly higher scattering intensities are observed for HC-2 in the scattering vector (Q) region of 0.1–0.2 Å^{-1}, indicating a larger amount of pores with diameters of 1.5–3.0 nm. Assuming spherical pores, these SAXS patterns are fitted by the equations (Eq. (5) and (6)) as follows:[28]

$$I(Q, R_0, M) = \int_0^\infty |F(Q,R)|^2 P(R) \frac{1}{R^3}\, dR \quad (5)$$

$$P(R) = \frac{1}{\Gamma(M)} \left(\frac{M}{R_0}\right)^M e^{-\frac{M}{R_0}R} R^{-1+M} \quad (6)$$

where R is the radius of pores, R_0 is the average radius of pores, M is shape parameter, $I(Q, R_0, M)$ is the intensity of the SAXS pattern, $F(Q, R)$ is the form factor, $P(R)$ is the pore size distribution function, and $\Gamma(M)$ is the gamma function. Figure 3b shows the pore diameter distributions obtained from the SAXS patterns. HC-2 shows a higher probability in the region of pore diameters of 1–2 nm, resulting in a larger average pore diameter. The average pore diameters (D_{pore} ($= 2R_0$)) are 1.22 and 1.31 nm for HC-1 and HC-2, respectively. Komaba et al. reported that the D_{pore} value of the same hard carbon as HC-1 was ~1.4 nm,[14] which is consistent with the data obtained in the present study. In addition, HC-1 possesses larger amounts of smaller pores less than 0.5 nm in diameter. Actually, the shape parameter (M) of HC-1 and HC-2 are 2.95 and 2.89, respectively, indicating that HC-1 has a slightly wider pore size distribution width. One of the main purposes of the present study is to investigate the correlation between pore size distribution and charge–discharge behavior, the details will be discussed in the next section.

3.1.4 Morphology observation by FE-SEM

Figure 4 shows representative FE-SEM images of HC-1 and HC-2. Relatively large secondary particles with diameters of ~20 μm are

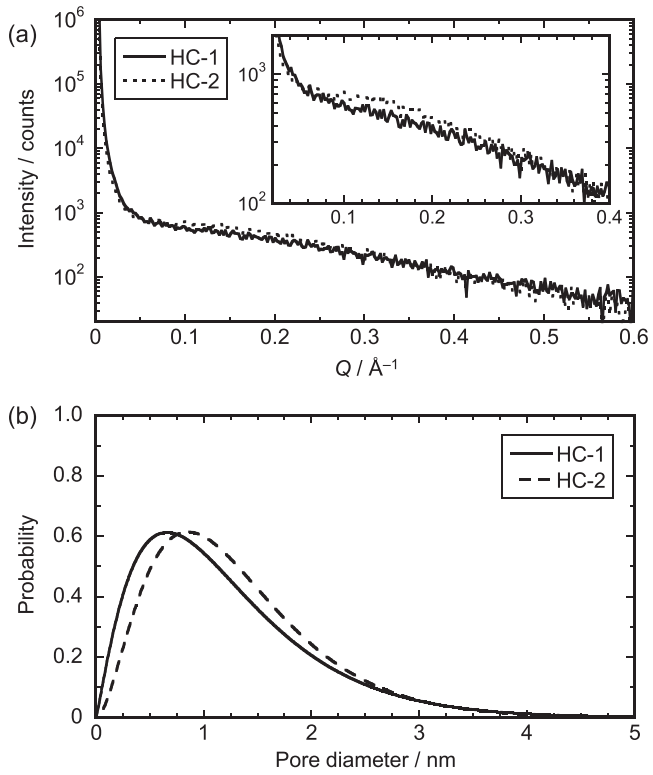

Figure 3. (a) SAXS patterns and (b) pore diameter distributions of HC powders.

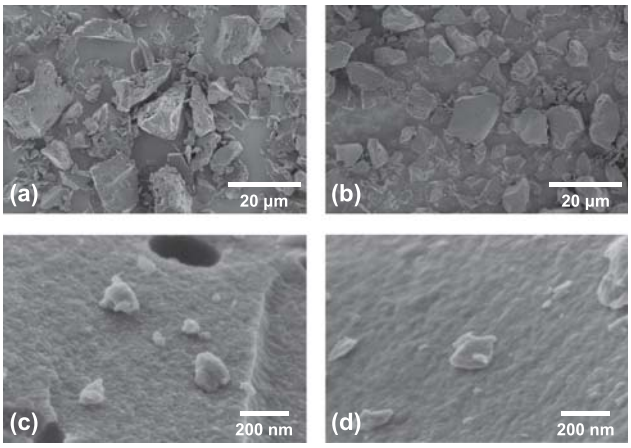

Figure 4. FE-SEM images of HC powder at different magnifications. (a) HC-1 and (b) HC-2 at lower magnification; (c) HC-1 and (d) HC-2 at higher magnification.

observed for both HCs. At higher magnification (Figs. 4c and 4d), smaller secondary particles of ~200 nm diameter are observed on the surface of larger HC particles. In addition, the small bumps on the surface with a size of ~30 nm are likely to be primary particles, which is consistent with the results of Raman spectroscopy.

3.2 Charge–discharge characteristics of HC electrodes

3.2.1 Charge–discharge behavior at low current density

Figures 5a and 5b show galvanostatic charge–discharge curves of HC-1 and HC-2 at a current density of 50 mA (g-HC)$^{-1}$. Both HC electrodes exhibit typical charge–discharge behavior, with a slope region appearing at 0.2–0.7 V and a plateau region below ~0.2 V, which has already been reported for the tests in organic solvent-based electrolytes.[12–14,16] The mechanism of sodium insertion/deinsertion proposed for the organic solvent-based electrolytes is

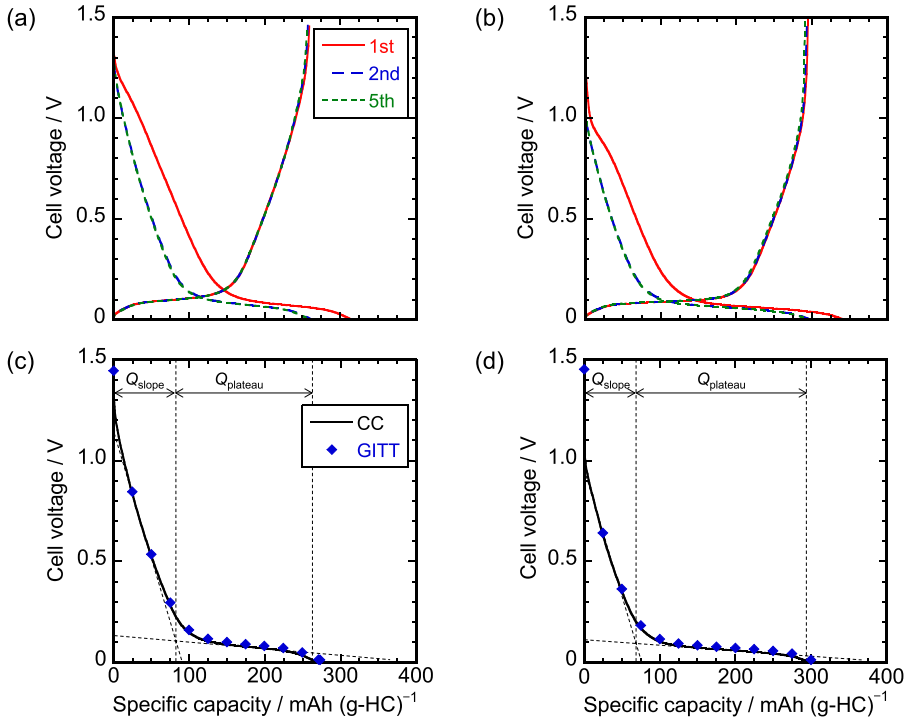

Figure 5. (Color online) Galvanostatic charge–discharge curves of (a) HC-1 and (b) HC-2 for 1st, 2nd, and 5th cycles. Comparison between the 5th charge curves (solid curves) at constant current (CC) mode and GITT plots (diamond symbols) for (c) HC-1 and (d) HC-2. For CC mode, the current density and the voltage range were 50 mA (g-HC)$^{-1}$ and 0.005–1.500 V, respectively. The conditions and procedure for GITT are described in section 2.2. Operating temperature: 363 K.

likely to be applicable to the present ionic liquid electrolyte, i.e., the slope and plateau regions correspond to sodium insertion/deinsertion between the graphene sheets and in the interstitial sites of graphene domains (pores), respectively.[12–14,16] In the first cycle, HC-1 and HC-2 exhibit the discharge (desodiation) capacities of 259 and 295 mAh (g-HC)$^{-1}$, and their coulombic efficiencies are 82.7 and 86.7%, respectively. Since the small plateau of ~50 mAh (g-HC)$^{-1}$ at around 1.0 V during the 1st charge (sodiation) is not observed in the 2nd cycle, this capacity is considered to originate from the irreversible decomposition of the ionic liquid electrolyte and the formation of solid electrolyte interphase (SEI). Several groups have reported the SEI formation in ionic liquid electrolytes.[29–31] In the case of silicon negative electrodes for LIBs using Li[FSA]–[C_3C_1pyrr][FSA] ionic liquid,[29] XPS analysis suggested the formation of LiF, sulfates, sulfites, and sulfides. Other group reported that LiF was detected on the surface of lithium metal immersed in [C_3C_1pyrr][FSA] ionic liquid by X-ray diffraction.[30] Recently, our group also investigated the stability of sodium metal in imidazolium-based ionic liquids, and proved the formation of NaF on the surface of sodium metal immersed in Na[TFSA]–[C_2C_1im][TFSA] ionic liquid.[31] Thus, NaF is one of the most probable compounds in the SEI layer in the present study using Na[FSA]–[C_3C_1pyrr][FSA] ionic liquid electrolyte. However, detailed studies are necessary in the future. Both HC-1 and HC-2 show good cycling characteristics for initial 5 cycles, with the discharge capacities in the 5th cycle being 256 and 291 mAh (g-HC)$^{-1}$ for HC-1 and HC-2, respectively.

Figures 5c and 5d show the comparison of charge curves in the 5th cycle and the open circuit potentials obtained by the galvanostatic intermittent titration technique (GITT). The GITT plots were obtained after the galvanostatic charge–discharge tests for 4 cycles. As a result, the GITT plots overlap the charge curves for both HC-1 and HC-2, suggesting that the current density of 50 mA (g-HC)$^{-1}$ is small enough to realize the quasi-equilibrium state of HC electrodes.

Incidentally, for practical application, information on charge–discharge behavior at room temperature is also important. As the results of charge–discharge tests at a current density of 50 mA (g-HC)$^{-1}$ at 298 K, discharge capacities of HC-1 and HC-2 are 72 and 49 mAh (g-HC)$^{-1}$, respectively, which are lower than those at 363 K. However, at a low rate of 10 mA (g-HC)$^{-1}$, their capacities increase to 222 and 225 mAh (g-HC)$^{-1}$, respectively, indicating that these HCs are operable in Na[FSA]–[C_3C_1pyrr][FSA] ionic liquid at a wide temperature range of 298–363 K.

3.2.2 Correlation between the capacity and structure of HCs

A closer look at the charge–discharge curves (Figs. 5c and 5d) reveals that the capacities of slope and plateau regions are different for HC-1 and HC-2. Thus, to clarify this behavior, these capacities were determined by extrapolating the approximate straight lines of the two regions, i.e., the capacity at the intersection of these two lines was assumed to be the slope-region capacity (Q_{slope}), and the remaining capacity was regarded as the plateau-region capacity ($Q_{plateau}$). The calculated capacities are summarized in Table 1. HC-1 shows larger Q_{slope} and smaller $Q_{plateau}$ than HC-2. Since sodium is inserted between the graphene sheets in the slope region,[12–14,16] it is reasonable to consider that the slope-region capacity is related to the interlayer distance of graphene sheets. The comparison of d_{002} and Q_{slope} values naturally leads to the conclusion that HC with a larger d_{002} value shows a higher capacity.[19] Concerning the plateau region, larger D_{pore} gives higher $Q_{plateau}$ values, which is consistent with the previous studies conducted in organic solvent-based electrolytes.[20] Moreover, HC-1 has smaller pores of $D_{pore} < 0.5$ nm (See Fig. 3b) and showed the lower $Q_{plateau}$ value, suggesting that these small pores do not contribute to the practical capacity.

3.2.3 Rate properties

Figures 6a and 6b show the rate capabilities of HC electrodes at current densities of 50–2000 mA (g-HC)$^{-1}$. Both electrodes show similar behavior, and the plateau regions disappear at current densities over 500 mA (g-HC)$^{-1}$, resulting in substantial capacity decrease. The plateau potential is close to the cut-off voltage of the

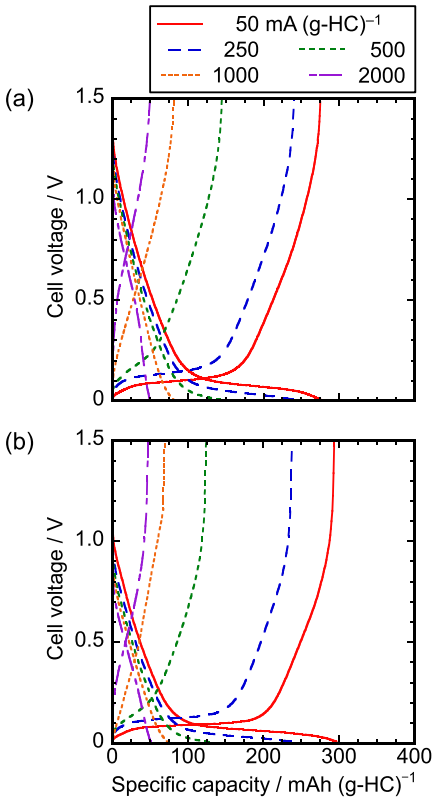

Figure 6. (Color online) Galvanostatic charge–discharge curves of (a) HC-1 and (b) HC-2 at current densities of 50–2000 mA g^{-1} in the voltage range of 0.005–1.500 V at 363 K.

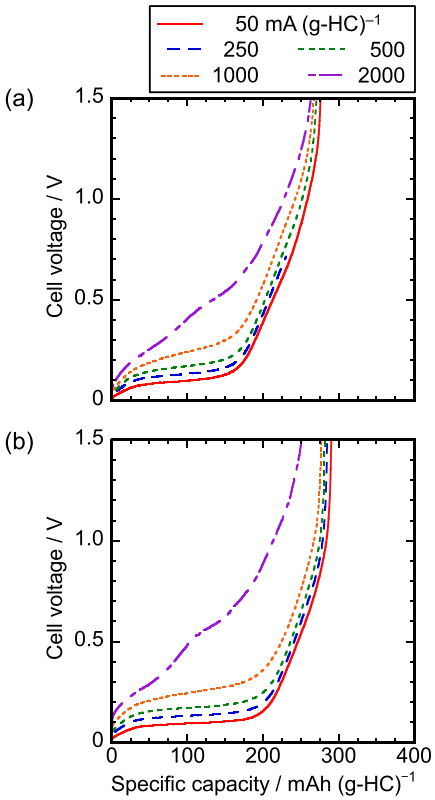

Figure 7. (Color online) Galvanostatic discharge curves of (a) HC-1 and (b) HC-2 at current densities of 50–2000 mA (g-HC)$^{-1}$ in the voltage range of 0.005–1.500 V at 363 K. Charging current density was fixed at 25 mA (g-HC)$^{-1}$.

charge process (0.005 V), which is reached before the plateau region starts. As a result, $Q_{plateau}$ cannot be utilized at current densities over 500 mA (g-HC)$^{-1}$. Although high coulombic efficiencies of over 99.7% are obtained at all current densities for HC-1, those for HC-2 decrease with increasing current densities (from 99.0% at 50 mA (g-HC)$^{-1}$ to 92.5% at 2000 mA (g-HC)$^{-1}$). These results suggest that HC-2 possesses inferior discharge rate capabilities compared to HC-1.

To confirm this hypothesis, the discharge rate capabilities were investigated under a minimized charge current density of 25 mA (g-HC)$^{-1}$. Figures 7a and 7b show the discharge curves of HC-1 and HC-2, respectively, at discharge current densities of 50–2000 mA (g-HC)$^{-1}$. HC-1 shows reasonably high discharge rate capabilities, maintaining a high capacity of 263 mAh (g-HC)$^{-1}$ even at a large current density of 2000 mA (g-HC)$^{-1}$, which is equivalent to 95% of the capacity at 50 mA (g-HC)$^{-1}$. Although HC-2 shows similar behavior at current densities below 1000 mA (g-HC)$^{-1}$, its capacity suddenly decreases to 251 mAh (g-HC)$^{-1}$ at 2000 mA (g-HC)$^{-1}$, corresponding to 86% of the capacity at 50 mA (g-HC)$^{-1}$. Compared to HC-1, the large polarization observed for HC-2 in the plateau region at 2000 mA (g-HC)$^{-1}$ suggests that sodium deinsertion from pores is the rate-determining step, and the larger polarization originates from the smaller average pore size of HC-2.

3.2.4 Cycling properties

Figure 8 summarizes the cycling properties of HC-1 and HC-2 at a current density of 250 mA (g-HC)$^{-1}$ over 300 cycles. HC-1 shows stable discharge capacities above 220 mAh (g-HC)$^{-1}$ for 300 cycles and high coulombic efficiencies above 99.8% except the initial few cycles. HC-2 also exhibits high capacities above 250 mAh (g-HC)$^{-1}$ and high average efficiencies of 99.9% except the initial few cycles. The HC-1 and HC-2 capacity retention ratios after 300 cycles (ε) are 95.6 and 89.2%, respectively, as calculated from the following equation:

$$\varepsilon = \left(\frac{Q_{300}}{Q_{max}}\right) \times 100 \qquad (7)$$

where Q_{max} is the maximum discharge capacity for 300 cycles and Q_{300} is the discharge capacity at the 300th cycle. Although no significant shape change of charge–discharge curves is observed for both HC-1 and HC-2, the charge and discharge curves of HC-2 slightly shift toward lower and higher voltages, respectively, with increasing cycle number. Thus, the larger capacity decrease is observed for HC-2 after 300 cycles.

4. Conclusions

In this study, hard carbons (HCs) were investigated as negative electrodes for sodium secondary battery utilizing the Na[FSA]–[C_3C_1pyrr][FSA] ionic liquid electrolyte at 363 K, and the correlation between charge–discharge behavior and structural properties was studied.

First, the structural properties of two HC powders (HC-1 and HC-2) were analyzed, with HC-1 showing slightly larger d_{002} and smaller D_{pore} values. Both HC electrodes exhibited typical hard carbon charge–discharge behavior, with capacities above 250 mAh (g-HC)$^{-1}$ at 50 mA (g-HC)$^{-1}$. HC-1, having a larger d_{002} value, showed a higher Q_{slope} value, while HC-2, showing a larger D_{pore}, exhibited a higher $Q_{plateau}$ value during the charge process. The mechanism of sodium insertion in the ionic liquid electrolyte is essentially the same as that in organic solvent-based electrolytes.

The rate capabilities and cycling properties were also evaluated. The capacity substantially decreased at charge current densities above 500 mA (g-HC)$^{-1}$. On the other hand, stable discharge rate capabilities up to 2000 mA (g-HC)$^{-1}$ were obtained when the charge current density was fixed at 25 mA (g-HC)$^{-1}$. Finally, both HC

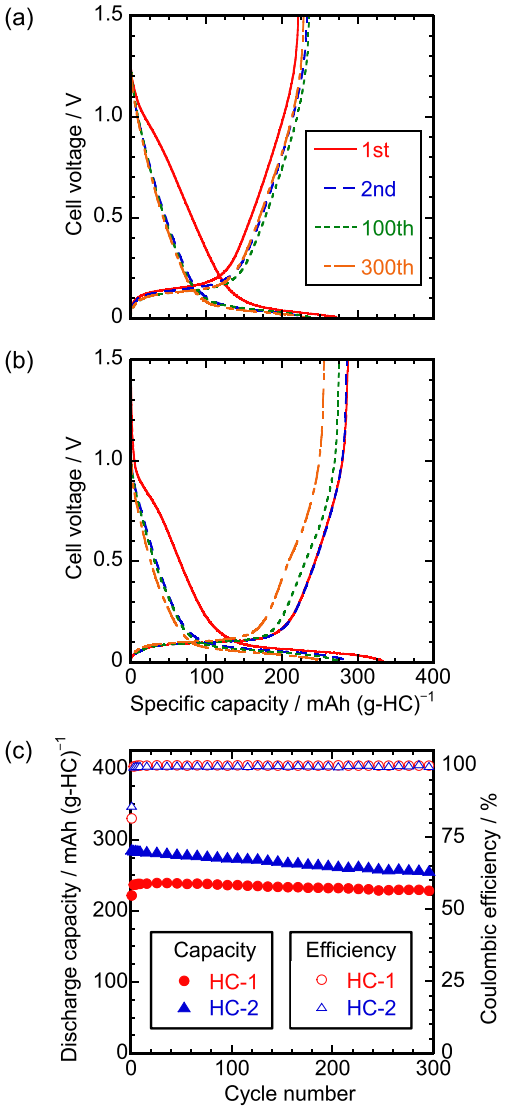

Figure 8. (Color online) Galvanostatic charge–discharge curves of (a) HC-1 and (b) HC-2 at current density of 250 mA (g-HC)$^{-1}$ in the voltage range of 0.005–1.500 V at 363 K. (c) Cycling properties of discharge capacities and coulombic efficiencies for HCs.

electrodes showed reasonably stable cycling properties, with coulombic efficiencies higher than 99.8% and capacity retention higher than 89% maintained for 300 cycles.

Acknowledgments

This study was partly supported by the Advanced Low Carbon Technology Research and Development Program (ALCA) of Japan Science and Technology Agency (JST), and MEXT program "Elements Strategy Initiative to Form Core Research Center" (since 2012), MEXT; Ministry of Education Culture, Sports, Science and Technology, Japan.

References

1. R. Hagiwara, K. Tamaki, K. Kubota, T. Goto, and T. Nohira, *J. Chem. Eng. Data*, **53**, 355 (2008).
2. T. Nohira, T. Ishibashi, and R. Hagiwara, *J. Power Sources*, **205**, 506 (2012).
3. K. Kubota, T. Nohira, and R. Hagiwara, *J. Chem. Eng. Data*, **55**, 3142 (2010).
4. A. Fukunaga, T. Nohira, Y. Kozawa, R. Hagiwara, S. Sakai, K. Nitta, and S. Inazawa, *J. Power Sources*, **209**, 52 (2012).
5. C. Ding, T. Nohira, K. Kuroda, R. Hagiwara, A. Fukunaga, S. Sakai, K. Nitta, and S. Inazawa, *J. Power Sources*, **238**, 296 (2013).
6. K. Matsumoto, Y. Okamoto, T. Nohira, and R. Hagiwara, *J. Phys. Chem. C*, **119**, 7648 (2015).
7. C. Y. Chen, K. Matsumoto, T. Nohira, C. Ding, T. Yamamoto, and R. Hagiwara, *Electrochim. Acta*, **133**, 583 (2014).
8. C. Ding, T. Nohira, A. Fukunaga, and R. Hagiwara, *Electrochemistry*, **83**, 91 (2015).
9. C. Y. Chen, K. Matsumoto, T. Nohira, and R. Hagiwara, *J. Electrochem. Soc.*, **162**, A176 (2015).
10. A. Fukunaga, T. Nohira, R. Hagiwara, K. Numata, E. Itani, S. Sakai, K. Nitta, and S. Inazawa, *J. Power Sources*, **246**, 387 (2014).
11. C. Ding, T. Nohira, R. Hagiwara, A. Fukunaga, S. Sakai, and K. Nitta, *Electrochim. Acta*, **176**, 344 (2015).
12. D. A. Stevens and J. R. Dahn, *J. Electrochem. Soc.*, **147**, 1271 (2000).
13. D. A. Stevens and J. R. Dahn, *J. Electrochem. Soc.*, **148**, A803 (2001).
14. S. Komaba, W. Murata, T. Ishikawa, N. Yabuuchi, T. Ozeki, T. Nakayama, A. Ogata, K. Gotoh, and K. Fujiwara, *Adv. Funct. Mater.*, **21**, 3859 (2011).
15. X. Xia and J. R. Dahn, *J. Electrochem. Soc.*, **159**, A515 (2012).
16. J. Zhao, L. Zhao, K. Chihara, S. Okada, J. Yamaki, S. Matsumoto, S. Kuze, and K. Nakane, *J. Power Sources*, **244**, 752 (2013).
17. K. Gotoh, T. Ishikawa, S. Shimadzu, N. Yabuuchi, S. Komaba, K. Takeda, A. Goto, K. Deguchi, S. Ohki, K. Hashi, T. Shimizu, and H. Ishida, *J. Power Sources*, **225**, 137 (2013).
18. M. Dahbi, T. Nakano, N. Yabuuchi, T. Ishikawa, K. Kubota, M. Fukunishi, S. Shibahara, J. Y. Son, Y. T. Cui, H. Oji, and S. Komaba, *Electrochem. Commun.*, **44**, 66 (2014).
19. G. Hasegawa, K. Kanamori, N. Kannari, J. Ozaki, K. Nakanishi, and T. Abe, *ChemElectroChem*, **2**, 1917 (2015).
20. B. Zhang, C. M. Ghimbeu, C. Laberty, C. Vix-Guterl, and J. M. Tarascon, *Adv. Energy Mater.*, **6**, (2016).
21. N. Iwashita, C. R. Park, H. Fujimoto, M. Shiraishi, and M. Inagaki, *Carbon*, **42**, 701 (2004).
22. The 117 Committee of the Japan Society for the Promotion of Sciences, *TANSO*, **221**, 52 (2006). [in Japanese]
23. M. D. Fang, T. H. Ho, J. P. Yen, Y. R. Lin, J. L. Hong, S. H. Wu, and J. J. Jow, *Materials*, **8**, 3550 (2015).
24. N. Iwashita, *TANSO*, **188**, 147 (1999). [in Japanese]
25. K. Kokaji, A. Oya, K. Maruyama, Y. Yamada, and M. Shiraishi, *Carbon*, **35**, 253 (1997).
26. L. G. Cançado, K. Takai, T. Enoki, M. Endo, Y. A. Kim, H. Mizusaki, A. Jorio, L. N. Coelho, R. Magalhães-Paniago, and M. A. Pimenta, *Appl. Phys. Lett.*, **88**, 163106 (2006).
27. M. A. Pimenta, G. Dresselhaus, M. S. Dresselhaus, L. G. Cançado, A. Jorio, and R. Saito, *Phys. Chem. Chem. Phys.*, **9**, 1276 (2007).
28. K. Omote, Y. Ito, and S. Kawamura, *Appl. Phys. Lett.*, **82**, 544 (2003).
29. D. M. Piper, T. Evans, K. Leung, T. Watkins, J. Olson, S. C. Kim, S. S. Han, V. Bhat, K. H. Oh, D. A. Buttry, and S. H. Lee, *Nat. Commun.*, **6**, 6230 (2015).
30. A. Budi, A. Basile, G. Opletal, A. F. Hollenkamp, A. S. Best, R. J. Rees, A. I. Bhatt, A. P. O'Mullane, and S. P. Russo, *J. Phys. Chem. C*, **116**, 19789 (2012).
31. T. Hosokawa, K. Matsumoto, T. Nohira, R. Hagiwara, A. Fukunaga, S. Sakai, and K. Nitta, *J. Phys. Chem. C*, **120**, 9628 (2016).